



Modeling the optical properties of Morpho-inspired thin-film interference filters on structured surfaces

ANDREAS WESSELS,^{*}  ADRIAN CALLIES,  BENEDIKT BLÄSI, 
THOMAS KROYER, AND OLIVER HÖHN 

Fraunhofer Institute for Solar Energy Systems, Heidenhofstraße 2, 79110 Freiburg, Germany

^{*}andreas.wessels@ise.fraunhofer.de

Abstract: We present a method for modeling the optical properties of interference layer systems on structured surfaces as used in the MorphoColor technology for coloring integrated photovoltaic modules. By combining a microfacet-based bidirectional scattering distribution function model with a transfer matrix formalism, we can simulate the spectrally resolved reflection and transmission properties of the system in good agreement with measurement data. To consider the MorphoColor technology in an overall optical system and compare the application on the front side of the module glass with the application in the composite, the model is additionally combined with a formalism called Optical Properties of Textured Optical Sheets. For a representative illumination and viewing geometry, the composite configuration causes a significantly improved homogeneity of the color appearance.

© 2022 Optica Publishing Group under the terms of the [Optica Open Access Publishing Agreement](#)

1. Introduction

Photovoltaics (PV) plays a crucial role in the globally required transformation towards an energy system consisting exclusively of renewable sources. Building integrated PV (BIPV) has particularly great potential in this context and must be greatly expanded. In order to realize this practically, it is necessary to design BIPV products in an aesthetically way and to make them applicable as an active design element of the building envelope. A promising way to promote the acceptance and thus the integration of BIPV products into our built environment is colored PV. Architects, building planners and building owners are demanding solar components in individually selectable saturated colors that have a homogeneous appearance for all lighting respectively viewing angles. Additionally, they should help to avoid glare and at the same time have a high module efficiency. In the past, several concepts for the color design of BIPV products have been presented and included both cell-level and module-level solutions. An overview is given in [1–3]. Important examples of color generation by manipulating the module cover glass are briefly summarized here to show their possibilities as well as limitations. One possibility is printing the module glass with inks or ceramic pastes as well as the use of colored encapsulations. However, saturated colors can only be realized by a high shading of the PV cells and thus high efficiency losses [4]. Another concept is based on the introduction of selectively scattering films into the module. Various low-saturation colors as well as white can be realized, though the broadband reflection leads to high losses [5]. Previous products based on spectrally selective interference systems on the planar module glass allow only low-saturated pastel shades [6,7] or need a very thick layer stack to achieve high color saturation [8]. Furthermore they exhibit inflexible production of different colors due to their very different layer systems [6].

An approach that overcomes the problems of previous concepts by providing a broad range of saturated colors with a low angular dependence while maintaining high module efficiency and at the same time allows one to easily scale industrial production is the MorphoColor approach [9]. Its physical principles are described in [10]. The MorphoColor concept is inspired by the

complex 3D photonic structures found on the wing scales of the Morpho butterfly, which feature highly saturated colors with low angular dependence [11,12]. The biological structures consist of multiple ridges with lamellae branching off to both sides. Such structures can be effectively reproduced by depositing a Bragg stack on a rough substrate using sputter coating. In their investigation, Bläsi et al. [10] focus on the thin film aspect of the Morpho effect and mainly consider planar Bragg stacks. In this way, they show that the Morpho structure found in nature can be modified for enhanced color saturation and stability by using higher harmonic reflection orders (harmonic configuration) and a high average refractive index of the Bragg stack with Si_3N_4 as the low refractive and TiO_2 as the high refractive index material.

However, for the overall consideration of the Morpho effect, the angular distribution is a critical component and the scattering effects associated with a textured surface, as well as shadowing and masking, must be considered for a comprehensive view. Therefore, the scope of this work is a detailed analysis of the interactions between the thin film stack and the structure given by the substrate. We present a numerical approach using a microfacet-based BSDF model in combination with a transfer matrix formalism. With this, we derive a complete methodology for determining the reflectance and transmittance properties of rough coated substrates based on 3D structural characteristics as input. We validate the simulation data with measured data from two coated glasses with different surface structures and use the model to infer causal relationships between the structure, the layer stack, and the resulting spectral properties. Finally, we combine the model with the formalism called Optical Properties of Textured Optical Sheets (OPTOS) to be able to describe entire optical systems consisting of incoherently coupled layers and thus draw conclusions about the Morpho effect within an entire PV module.

2. Sample preparation, measurements, and preprocessing

2.1. Topographic measurements of uncoated structured glasses

To quantify the structural features of the etched glasses determining their scattering behavior, 3D surface measurements are performed. An Olympus 3D Measuring Laser Microscope LEXT OLS4000 is used for this purpose. To obtain reliable data, it is crucial to find a balance between a sufficiently large measurement area (statistical scope) and a sufficiently high resolution. For the structures examined here, stitching mode is used to obtain a total measurement area of approximately $580\text{ }\mu\text{m} \times 580\text{ }\mu\text{m}$ with a measurement point spacing of 125 nm using the 100x objective lens. These parameters combine a high resolution with representative statistics and provide the optimal result for the structures under investigation in contrast to, for example, smaller measuring areas. Before the resulting 3D data is used to calculate the occurring polar slope angles, a plane fit is carried out to compensate for any unintentional inclination of the sample during the measurement.

2.2. Application and initial investigation of the layer stack

The coating of the glass substrates is realized in an Interpane E&B custom-made sputtering machine using MF Magnetron sputtering. Dual rotatable tube cathodes are used for all materials. The configuration of the layer stack is the same as in [10] and consists of Si_3N_4 , TiO_2 , Si_3N_4 , TiO_2 , Si_3N_4 and SiO_2 , starting from the glass substrate.

To determine the refractive indices of the layered materials used, corresponding individual layers are deposited on glass substrates and/or Si wafers and the spectral reflectance and transmittance are measured by Fourier spectrometry. The refractive index data are then fitted to the measured data via the exponential Cauchy model.

For the determination of the individual layer thicknesses of an applied layer stack, a flat glass substrate is co-coated in each case. The reflectance and transmittance spectra of this reference are determined by Fourier spectrometry, after which the layer thicknesses are fitted using the

transfer matrix formalism. When referring to layer thicknesses in this work, we always mean physical thickness.

In both cases the optical measurement is carried out using a Bruker VERTEX 80 Fourier spectrometer equipped with an integrating sphere.

2.3. Angle-dependent reflection measurements

To suppress back-surface reflections in the angle-dependent reflection measurements, the glasses are blackened on the unstructured back side by means of a highly absorbent spray coating (Nigrin 74117). The two sample setups used for the angle-dependent measurements are schematically shown in Fig. 1.

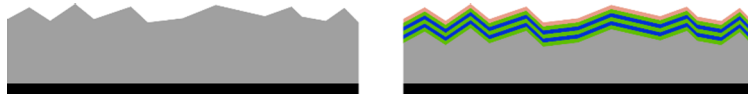


Fig. 1. Schematic illustration of the samples for the angle-dependent measurements. Left: Front side structured and uncoated glass in gray with absorbing spray coating in black on the flat rear side. Right: As on the left, but with the layer stack on the structured front side of the glass. The layer stack is shown with green for Si_3N_4 , blue for TiO_2 and coral for SiO_2 .

An Agilent Cary 5000 spectrometer is used in two different measurement configurations to measure the angle-dependent reflectance spectra. In both cases, the light is incident directly on the sample at a selectable angle. For measurements of reflectance into a cone with central direction in the plane of incidence and 6° half angle, the Cary Universal Measurement Accessory (UMA) is connected. For hemispherical reflectance measurements, the diffuse reflectance accessory (DRA) with center mount inside an integrating sphere is used instead. A schematic illustration of the two measurement configurations is shown in Fig. 2.

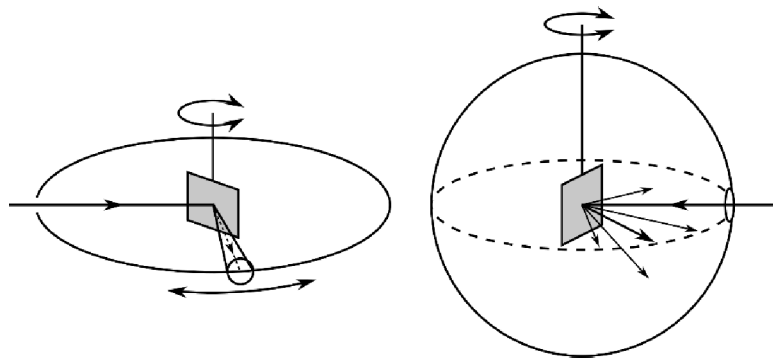


Fig. 2. Schematic illustration of the two measurement configurations of the Agilent Cary 5000. Left: Angle of incidence and angle of reflection dependent reflection measurement into a cone with 6° half angle. The sample shown in gray can be rotated around its vertical axis for setting the angle of incidence. The detector can be moved around the sample in the plane of incidence to define the observed angle of reflection. Right: Incidence angle dependent hemispherical reflectance measurement with center mount in the integrating sphere. To adjust the angle of incidence, the sample can be rotated around its vertical axis.

3. Models and model combinations

The etched glass structures used for the MorphoColor approach described in [10] are two orders of magnitude larger than the Morpho structure as found in nature. With a correlation length of

155 μm for glass A and 78 μm for glass B, this also applies to the two structures investigated here, whose microscope images can be seen in Fig. 5. The given correlation lengths are defined as the first value $> 0 \mu\text{m}$ at which the radial autocorrelation function assumes a relative maximum. Considering the structure sizes, in this work a purely ray-optical model is chosen to describe the scattering distribution. Further investigations with sub-micrometer structures are beyond the scope of this work and will be addressed in future work.

Figure 3 schematically shows the procedure required for the overall description of an optical system including the MorphoColor technology. These are presented in the following.

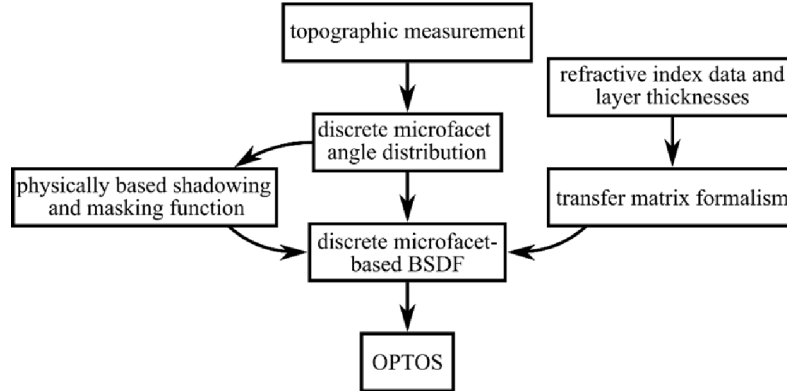


Fig. 3. Schematic visualization procedure used to describe the MorphoColor technology in an optical system.

3.1. Determination of the occurring polar angles

To calculate the polar angles θ_m of the structural elements from the 3D structural characteristics, a triangle (so-called microfacet) is created from three neighboring measurement points. The normal vector is determined via the vector product of the gradients g_x and g_y spanning the respective microfacet. The polar angle of the microfacet then corresponds to the angle between this normal vector N_m and the normal of the macrosurface N_M as shown in Fig. 4.

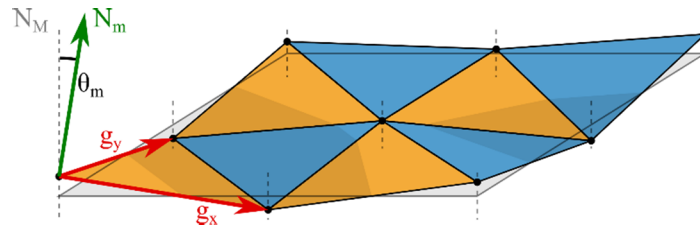


Fig. 4. Schematic illustration of the determination of the polar angles of the microfacets. The plane macrosurface is shown in gray. The elevation data at the respective measurement points are drawn as black dots and the resulting triangular microfacets are shown in blue and orange. As an example, the gradients g_x and g_y are drawn for one facet. Additionally, the microfacet normal vector N_m and the polar angle θ_m , which is spanned between N_m and the normal of the macrosurface N_M , are shown.

This process is carried out for all possible facets that can be spanned between four neighboring data points. A discretization into 360 possible bins is chosen for the polar angles obtained. The resulting one-dimensional normalized histogram of the occurring polar angles corresponds

to the discrete microfacet angle distribution $D(\theta_m)$, which serves as input parameter in the microfacet-based BSDF model.

3.2. Derivation of a discrete microfacet-based BSDF

The approach of considering specular reflections on individual microfacets to describe the reflectance of a rough surface to a particular angle dates back to the early 1920s [13]. On this basis, the microfacet model evolved both from the field of optical physics [14–16], and later through contributions from the field of computer graphics [17,18]. In the following derivation we follow the argumentation of Heitz [19] with one difference: Instead of an analytical microfacet distribution function we use a discrete angle distribution based directly on topographic measurement data. In accordance with Heitz, our derivation is based directly on the conservation of the visible projected area. This area is equivalent to the macrosurface projected onto the incident direction:

$$A_{proj} = A_M \cdot \cos \theta_I \quad (1)$$

where A_M is the area of the macrosurface and θ_I is the incident angle. The visible surface, with a particular microfacet orientation projected onto the direction of incidence is:

$$A_{proj}(\theta_m, \varphi_m) = A_M \cdot G(\theta_I, \theta_m, \varphi_m) \cdot \frac{D(\theta_m)}{n_\varphi} \cdot \frac{\cos \theta_r}{\cos \theta_m} \quad (2)$$

where $D(\theta_m)$ is the microfacet angle distribution per polar angle. Because of the assumption of an isotropic etching structure, we decided to distribute the respective area fraction of the facets with a discrete polar angle isotropically over $n_\varphi = 1000$ azimuth angles. When choosing a value for n_φ , there is a tradeoff between computational time and accuracy. For the results presented here, as computation time was not a limiting factor, we chose a very high accuracy, where the angular increment is at least one order of magnitude smaller than sampling with the aperture. This allowed us to exclude a potential source for inaccuracies and use the same value for all considered configurations. For large parameter variations with many calculations, where computation time becomes a critical factor, n_φ can be reduced by conducting a convergence analysis for the specific configuration. $\cos \theta_r / \cos \theta_m$ are the associated projection factors with θ_r being the half angle between the vectors in incidence direction \mathbf{I} and reflection direction \mathbf{R} . $G(\theta_I, \theta_m, \varphi_m)$ represents the so-called shadowing function (geometric attenuation factor). This considers that, viewed from the direction of incidence, some facets may be occluded by the microsurface and thus not contribute to the projected area. When using a Smith microsurface profile [16], it is implied that there is no correlation between the height and angle θ_m of a microfacet. Consequently, the shadowing factor has no dependence on the microfacet orientation for facets whose normal vector \mathbf{m} spans an angle smaller than 90 degrees with the vector in the direction of incidence \mathbf{I} . Because the microsurface is not autocorrelated, the microfacet orientation dependent and hence local property of binary sorting out of facets facing away (G_{local}) and the microfacet orientation independent and hence distant property of shadowing probability (G_{dist}) are independent of each other. Accordingly, the shadowing function can be written as:

$$G(\theta_I, \theta_m, \varphi_m) = G_{local}(\theta_I, \theta_m, \varphi_m) \cdot G_{dist}(\theta_I) \quad (3)$$

The local property can be realized using a Heaviside function $\chi^+(a) = 1$ if $a > 0$ and 0 if $a \leq 0$ resulting in $G_{local} = \chi^+(\cos \theta_r)$. For the derivation of G_{dist} , the requirement for a physically based shadowing function is used, according to which the projection of the visible microsurface

and the projection of the macrosurface on the incidence direction are identical:

$$\cos \theta_I = \sum_{\theta_m \varphi_m} G(\theta_I, \theta_m, \varphi_m) \cdot \frac{D(\theta_m)}{n_\varphi} \cdot \frac{\cos \theta_r}{\cos \theta_m} \quad (4)$$

Using Eq. (3) we can replace $G(\theta_I, \theta_m, \varphi_m)$ in Eq. (4) and pull the independent G_{dist} out of the sum. After solving for G_{dist} we derive:

$$G_{dist}(\theta_I) = \frac{\cos \theta_I}{\sum_{\theta_m \varphi_m} \chi^+(\cos \theta_r) \cdot \frac{D(\theta_m)}{n_\varphi} \cdot \frac{\cos \theta_r}{\cos \theta_m}} \quad (5)$$

Substituting G_{local} and G_{dist} into Eq. (3) yields the following for the shadowing function:

$$G(\theta_I) = \chi^+(\cos \theta_r) \cdot \frac{\cos \theta_I}{\sum_{\theta_m \varphi_m} \chi^+(\cos \theta_r) \cdot \frac{D(\theta_m)}{n_\varphi} \cdot \frac{\cos \theta_r}{\cos \theta_m}} \quad (6)$$

Analogous to the viewing from the direction of incidence, some facets may also be occluded by the microsurface when viewed from the direction of reflection, which is referred to as masking. Due to the reversibility of the light paths in a bidirectional scattering distribution, the same factor G can be used for masking as for shadowing but depending on the reflection angle θ_R instead of θ_I . Assuming statistically independent shadowing and masking, separately calculated and subsequently multiplied shadowing and masking functions can be used [18].

Now, it shall be considered which fraction of the incident radiation is reflected at the facets with orientation (θ_m, φ_m) . This can be calculated as the product of the Fresnel reflectance $R_{Fres}(\theta_r, \theta_t)$ and the fraction of the visible projected surface that has this orientation:

$$R = R_{Fres}(\theta_r, \theta_t) \cdot \frac{A_{proj}(\theta_m, \varphi_m)}{A_{proj}} = \frac{R_{Fres}(\theta_r, \theta_t)}{\cos \theta_I} \cdot G(\theta_I) \cdot G(\theta_R) \cdot \frac{D(\theta_m)}{n_\varphi} \cdot \frac{\cos \theta_r}{\cos \theta_m} \quad (7)$$

Due to the structural symmetry of the surface interface, an equation for the transmittance can be established in an analogous way using the Fresnel transmittance $T_{Fres}(\theta_r, \theta_t)$ and setting the shadowing function dependent on the angle of transmission θ_T :

$$T = \frac{T_{Fres}(\theta_r, \theta_t)}{\cos \theta_I} \cdot G(\theta_I) \cdot G(\theta_T) \cdot \frac{D(\theta_m)}{n_\varphi} \cdot \frac{\cos \theta_r}{\cos \theta_m} \quad (8)$$

In the later comparison with measured data, the discrete reflection or transmission results are considered summed over a solid angle matching the detector aperture used in the respective measurement configuration.

3.3. Combination with the transfer matrix formalism

Using the Fresnel factor, the model describes the scattering behavior at interfaces between two media having different refractive indices. In our case the interface consists of an uncoated structured glass surface in a surrounding medium. In order to include the MorphoColor layer stack in the analysis, the microfacet model is combined with the transfer matrix formalism by replacing the Fresnel terms $R_{Fres}(\theta_r, \theta_t)$ and $T_{Fres}(\theta_r, \theta_t)$ in Eq. (7) and Eq. (8) by the reflectance or transmittance of the layer stack formulated according to [20]. Due to the different polar angles of the microfacets, the thickness of the coatings deposited on them varies. Assuming a fully directional coating normal to the macrosurface, the thickness on a slanted microfacet would be $\cos \theta_m \cdot t_0$ where t_0 is the thickness on a microfacet parallel to the macrosurface. However, due to the typically non-uniform angular distribution of the sputtered atoms [21], this assumption does not apply. Sputtering tests carried out in this respect on planar glass specimens with different

inclinations have shown that a layer growth assumed to be 56% directional and 44% isotropic agrees well with the determined thicknesses. The layer thickness on the respective microfacets is thus calculated as $t_m = ((1 - 0.56) + 0.56 \cdot \cos \theta_m) \cdot t_0$. It is important to emphasize that the ratio used is specific to the sputtering conditions and geometries in the sputtering system used here and is not universal.

3.4. Integration of the model combination into the OPTOS formalism

To incorporate the MorphoColor-coated textured substrate into a complex overall optical system, the OPTOS formalism (Optical Properties of Textured Optical Sheets) is used [22–24]. OPTOS allows for the incoherent coupling of any number of textured interfaces with arbitrary spatial regimes. Each individual interface can thus be computed using the most appropriate model and subsequently be discretized to a set of possible propagation directions valid for all interfaces. By representing the individual interfaces as equally dimensioned scattering and absorption matrices, complex optical systems can be efficiently modeled using simple matrix products, whereby multiple reflections between the individual interfaces are considered. For the discretization of the results from the microfacet model combined with the transfer matrix formalism, the partitioning of the half-space into the possible input and output channels proposed by Tucher et al. [23] is adopted.

4. Results and discussion

4.1. Discrete microfacet angle distribution for uncoated structured glasses

Figure 5 shows the 3D structural characteristics of the investigated glass structures A and B resulting from the topographic measurements. These serve as input data for the determination of the frequency distribution of the occurring polar angles depicted in Fig. 6. The frequency of occurrence is represented in proportionality per unit element of the solid angle. This representation is related to the distribution function $D(\theta_m)$ used above by the factor $1/(2\pi \cdot \cos(\theta) \cdot \sin(\theta))$ and is chosen here because it allows for an intuitive comparison with angle-dependent reflectance measurements. The determined polar angle distribution of glass A shows a form similar to a normal distribution with occurring angles up to about 19° . For glass B, the distribution deviates significantly and does not correspond to a normal distribution. A global maximum in the range of 0° is followed by a local maximum around 11° polar angle. From here, the distribution continues with a relatively flat decline and shows angles up to approximately 40° . The high frequency noise observed in both distributions is due to discrete binning in steps of 0.25° .

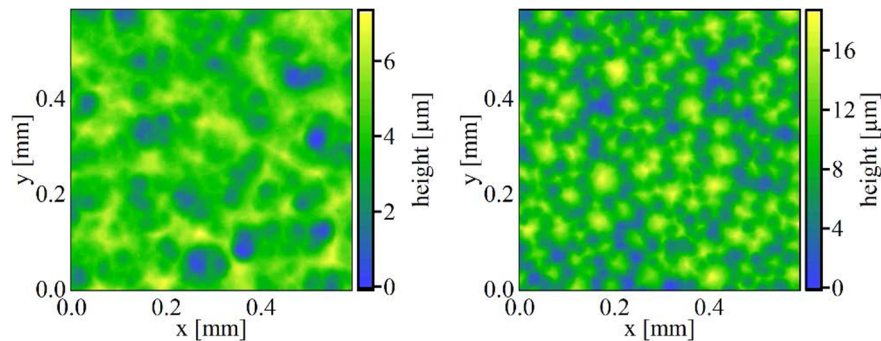


Fig. 5. Left: Laser Microscope image of the etched glass surface A. Right: Laser Microscope image of the etched glass surface B.

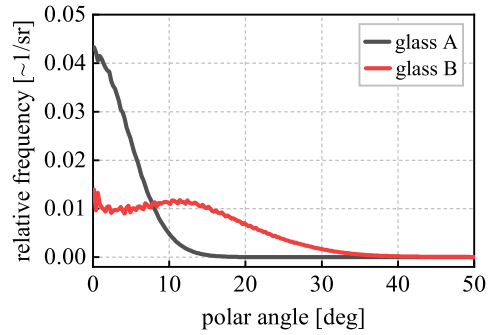


Fig. 6. Discrete microfacet polar angle frequency distributions of the investigated glass structures A and B plotted up to a polar angle of 50° .

4.2. Comparison of the discrete microfacet-based BSDF with angle-dependent reflectance measurements of uncoated structured glass

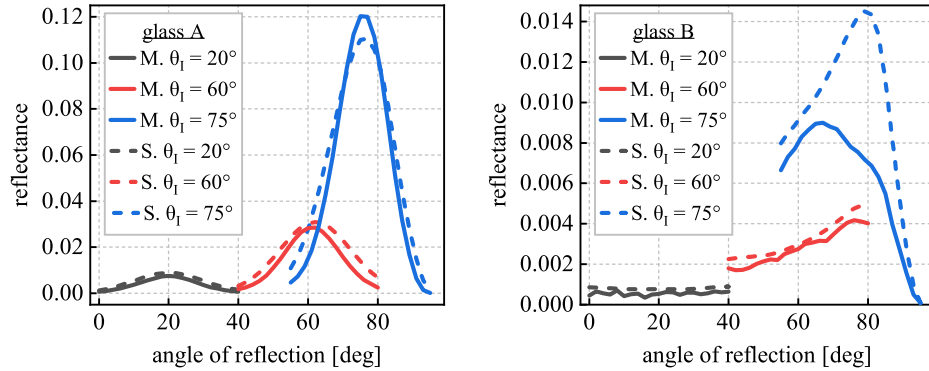


Fig. 7. Comparison of measured (M.) and simulated (S.) angle-dependent reflectance at incident angles of 20° , 60° and 75° at considered light wavelength of 500 nm. Left: For glass A. Right: For glass B.

Using the obtained angle distributions $D(\theta_m)$ as an input for the discrete microfacet-based BSDF model, the angle dependent reflection characteristics of uncoated glasses A and B are modeled and compared to measurement data. As can be seen in Fig. 7, the angle-dependent reflection behavior of both structured glasses can be well reproduced with a maximum deviation in the order of 1.5% (absolute) for glass A and 0.7% (absolute) for glass B. Except for the area around the direct reflection at an incidence angle of 75° for glass A, all simulation results show a systematic overestimation of the absolute reflection of the surface. In the case of glass A, this overestimation is relatively small overall, smallest at or near the direct reflection and increasing with distance from it. As can already be deduced from the polar angle distribution of the microfacets in Fig. 6, glass B does not show a form similar to a normal distribution and scatters much more widely than glass A. This results in comparatively very low intensities, which explains the noise in the measured data. For the angles of incidence of 20° and 60° , only very small deviations are shown for glass B as well. For light incidence of 75° however, the overestimation of the intensity becomes relatively large. A possible reason for this is that glass B shows a slight correlation between the height of the microfacets and their angles. In this case, large polar angles occur somewhat more frequently on higher facets. This correlation, which is neglected in the model, could lead to an error in which the model underestimates the shadowing

and masking. Especially for large angles of incidence where the influence of shadowing and masking increases.

4.3. Comparison of the combined discrete microfacet-based BSDF and transfer matrix formalism model with angle-dependent reflectance measurements of coated structured glasses

MorphoColor layer stacks resulting in a green color sputtered on glass A and B are simulated with the model combination. A comparison is made between angle-dependent reflectance measurements and simulation results. Exemplarily, the resulting spectra for glass A are plotted in Fig. 8. The spectral position of the main peak matches up to a maximum deviation of three nanometers. The overestimation of the reflection intensity already observed for uncoated glass can also be seen here. Consistent with the previous descriptions, the relative deviation increases when deviating from the direct reflex.

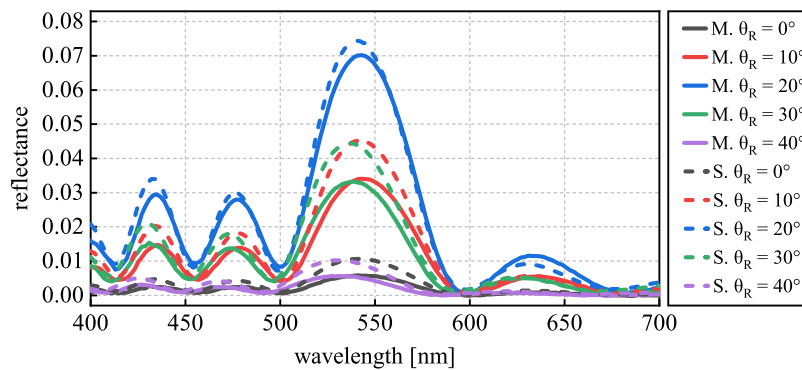


Fig. 8. Comparison of measured angle-dependent reflectance spectra (M.) at an incidence angle of 20° and different reflection angles and the corresponding simulation results (S.) for glass A.

In the application case for colored PV modules, it is crucial that the model combination reflects the color appearance well. Therefore, a consideration of the resulting color coordinates is carried out in the following. Figure 9 shows a good agreement between measurement and simulation for both glasses. At the same time, the graphs illustrate the fundamentally different behavior of glass A and B. Glass A shows a clear shift of the $L^*a^*b^*$ color coordinates over the selected angles, with a maximum near the direct reflection and, deviating from this, a decrease in saturation and lightness. For glass B, on the other hand, the values remain close together in the range of less strong saturation and lightness. The results thus fit well with the statements already made about the scattering behavior of the uncoated glasses.

To extend the consideration to areas of angular space further away from the previously considered regions intersecting the plane of incidence, a comparison of the measured and simulated hemispherically integrated reflectance spectra is performed and illustrated in Fig. 10 for glass A and in Fig. 11 for glass B. As a result, it allows for a more comprehensive comparison of scattering properties into the third dimension. In general, there is very good agreement between measurement and simulation, both in terms of absolute reflection and peak positions. Glass B shows slightly stronger quantitative differences between measurement and simulation but qualitatively the behavior matches very well also in this case. It is interesting to note that the systematic overestimation of intensity for light incident from large angles, previously observed in the angle-dependent measurements, does not occur in the hemispherical measurements. A valid explanation for this cannot be given at the moment.

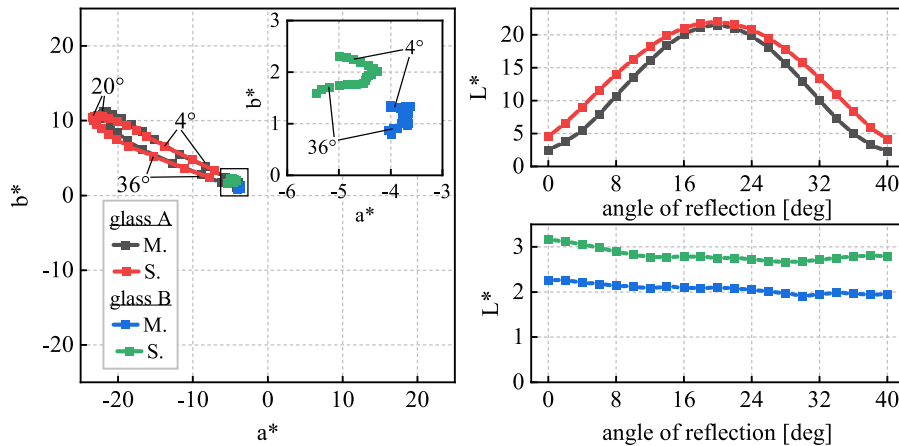


Fig. 9. Left: a^* b^* coordinates of the spectral data from angle-dependent reflectance measurements (M.) and simulations (S.) for glasses A and B at an incidence angle of 20° and reflection angles from 0° to 40° in steps of 2° . The insert shows the area relevant for glass B enlarged, with the data for glass A hidden for better clarity. In order to clarify the course of the a^* b^* coordinates over the angle of reflection, some data points are labeled with the corresponding angle. Right: Corresponding L^* values. All color coordinates in this work are calculated according to [25] with the CIE 10° standard colorimetric system.

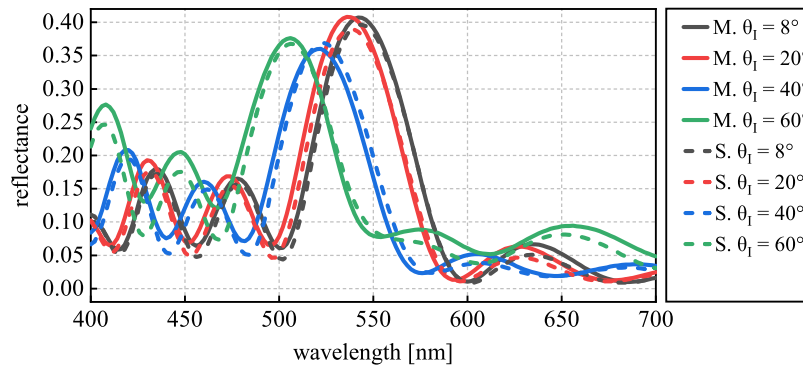


Fig. 10. Comparison of measured hemispherically integrated reflectance spectra (M.) at incidence angles of 8° , 20° , 40° , and 60° and corresponding simulation results (S.) for glass A.

The comparisons clearly show how well the model describes the effects occurring with structured substrates. In the case of the only slightly scattering structure on glass A, these effects are just small and the hemispherically integrated spectra correspond approximately to those of an observation on a flat substrate. For glass B, on the other hand, as an example of a more strongly scattering surface, the results differ significantly. Two main effects can be attributed to this. First, the light striking the sample is incident on facets with significantly larger angles. The angles of incidence with respect to the individual facets are therefore larger, which causes the reflected spectra to be shifted more strongly in the direction of smaller wavelengths (toward the blue). The hemispherically integrated spectrum thus appears shifted toward the blue as well. Second, this effect is further enhanced by the fact that the respective layer thicknesses on the microfacets become thinner the more inclined the facet is due to the directional dependence of the coating process. The thinner layers additionally lead to a blue shift of the reflected spectra.

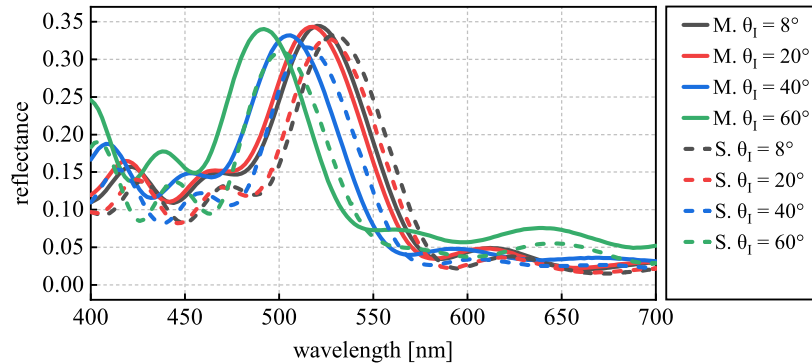


Fig. 11. Comparison of measured hemispherically integrated reflectance spectra (M.) at incidence angles of 8°, 20°, 40°, and 60° and corresponding simulation results (S.) for glass B.

Basically, the following can be summarized for the comparison of model and measurements:

1. The scattering behavior is well reproduced, but with a small systematic overestimation of the reflected intensity (except for the area around the direct reflection at an angle of incidence of 75° for glass A). Deviating from the direct reflex, the effect increases.
2. Reflection maxima and minima agree well with respect to their spectral position.
3. Fundamental effects of the MorphoColor technology are well explainable and qualitative estimations are well possible.
4. Quantitatively, the origin of the observed deviations must be further investigated.

4.4. Simulation of MorphoColor technology in a more complex optical system using OPTOS

For a more application-related consideration of the effects occurring through the MorphoColor technology, the next step is to consider the interaction with the interfaces present in the overall system. For this purpose, simulation results of the described model combination were used as input for an OPTOS-based comparison. The previous configuration with the layer stack on the front side (position 1), shown in Fig. 12 on the left side, is compared with a setup in which the layer stack is applied to the back side (position 2) of a cover glass structured on both sides, as depicted in Fig. 12 on the right side. The back of both configurations is calculated as fully absorbing as a simple but representative model for a PV module. The structures used are that of glass A.

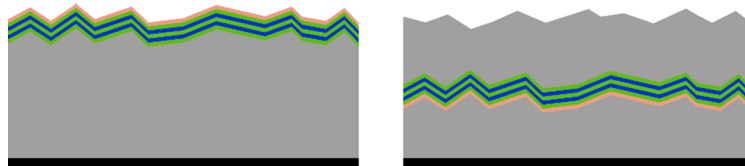


Fig. 12. Schematic illustration of the two configurations of the considered optical system. Color coding as in Fig. 1. Left: Layer stack on the front side of the structured glass (position 1). Right: Layer stack on the back side of a double-sided structured glass (position 2) followed by another glass and an index matched fully absorbing layer.

Figure 13 shows the a^*b^* evaluation on the left and the L^* evaluation on the right, resulting from the simulation of an entire MorphoColor installation under consideration, for example a building facade. The viewing geometry is visualized in Fig. 14 and a schematic color rendering is shown in Fig. 15.

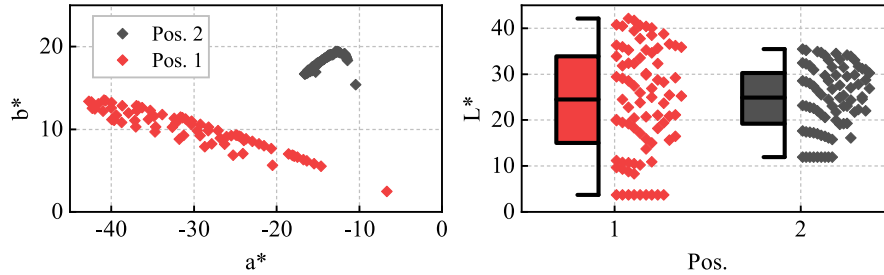


Fig. 13. Left: Comparison of the a^*b^* coordinates. Right: Comparison of the L^* coordinates in the form of boxplots with $Q1 = 25\%$, $Q2 = 75\%$ and a whisker definition of $\max. 1.5 \cdot IQR$. Both are calculated from OPTOS results from the simulation of a whole observed area of a MorphoColor facade for the position 1 (Pos. 1) and the position 2 (Pos. 2) configuration. The viewing angles used roughly represent a situation where an observer is on the street in front of the facade of a tall building. The light incidence is directly from $\theta_I = 30^\circ$ and $\varphi_I = 0^\circ$ whereby the coordinate system is chosen so that the x-axis corresponds to the facade vertical, the y-axis to the facade horizontal and the z-axis to the facade normal. The viewer can look up from his eye level 40° and sideways in both directions up to an angle of 40° . The step size of all angles is 5° . The observation takes place for each angle in a solid angle of 0.2 sr. A visualization of the observation situation can be seen in Fig. 14.

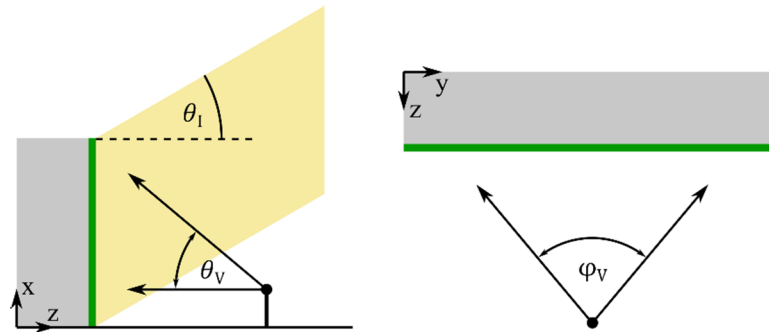


Fig. 14. Visualization of the observation situation for Fig. 13. Left: Side view with the building in gray and the MorphoColor facade in green. The angle of incidence of the light θ_I , as well as the range of possible viewing angles when looking up at the building θ_V from 0° on the eye level up to 40° are shown. Right: Top view with the building and the facade as before. Shown is the range of possible lateral viewing angles φ_V from 0° normal to the facade up to 40° both to the left and the right.

As can be seen quantitatively in Fig. 13 and visually in Fig. 15, both the saturation (chroma) and the lightness vary significantly less for the Pos. 2 than for the Pos. 1 configuration. This is probably caused by the additional scattering of the uncoated first glass interface in the Pos. 2 case, which contributes twice to the scattering of the reflected light. The stronger scattering distributes the reflection of the MorphoColor interface more homogeneously over the hemisphere. Although this reduces the absolute maximum values of chroma and lightness, their absolute minima increase at the same time. The result is a more homogeneous appearance overall. If the color difference

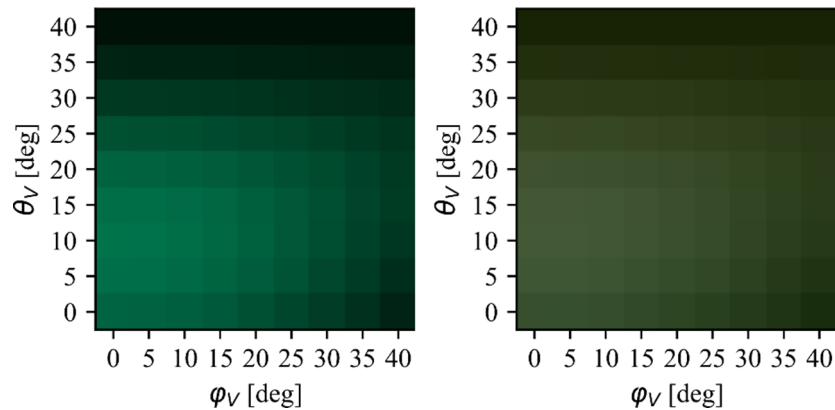


Fig. 15. Color rendering of the $L^*a^*b^*$ coordinates from Fig. 14 displayed as sRGB colors calculated according to [26] but using the appropriate transformation matrix for D65 reference white with 10° observer. Since the scattering for the viewing geometry under consideration is mirror-symmetrical for the view to the left and right, only one half ($\varphi_V = 0^\circ$ to $\varphi_V = 40^\circ$) is shown. Left: For position 1 configuration. Right: For position 2 configuration.

ΔE_{76} [25] is determined for Pos. 1 and Pos. 2 individually from all $L^*a^*b^*$ coordinates, the root mean square (RMS) ΔE_{76} for Pos. 1 is approximately 22.9 and for Pos. 2 a RMS ΔE_{76} of approximately 10.5 results. This clearly underlines the more homogeneous appearance of the Pos. 2 configuration and agrees qualitatively very well with practical observations on real samples.

5. Conclusion

In this work, we presented a model combination of a microfacet model and the transfer matrix formalism, with which the reflection and transmission behavior of interference layer systems applied to structured surfaces governed purely by ray-optics can be modeled and predicted. We describe the methodology to move from a topographic measurement of the surface structure to a spectrally resolved discrete BSDF, successively comparing with real measured data and showing a very good agreement. Beyond the consideration of the MorphoColor interface, we exemplified how the results of the presented model combination can be used as input for a more holistic consideration of the effects in a PV module using OPTOS. When comparing the MorphoColor technology at position 1 and 2, clear advantages were shown for position 2 regarding the angular stability of the color. For upcoming research and development concerning the selection of a surface texture, the presented model combination is a very good tool for evaluating different glass textures, as well as optimizing them with respect to a desired color behavior.

As an outlook for further research, a closer look at the observed deviations between measurement and simulation at larger angles can be mentioned. Likewise, the presented model must be tested with further structural characteristics. Furthermore, an adjustment of the geometric attenuation factor for textures with a strong correlation between the height and angle θ_m of a microfacet would be conceivable and interesting.

Funding. Bundesministerium für Wirtschaft und Energie (03EE1049A, 03ETW007A); Deutsche Bundesstiftung Umwelt.

Acknowledgments. The authors thank the Fraunhofer ISE colleagues Harald Lautenschlager and Tuuli Tetttenborn for helping with device processing and characterization. Special thanks also go to Dr. Andreas Gombert and Prof. Dr. Stefan Glunz for their helpful input, discussions and proof-reading. Andreas Wessels gratefully acknowledges scholarship support from the Deutsche Bundesstiftung Umwelt (DBU).

Disclosures. The authors declare no conflicts of interest.

Data availability. Data underlying the results presented in this paper are not publicly available at this time but may be obtained from the authors upon reasonable request.

References

1. T. E. Kuhn, C. Erban, M. Heinrich, J. Eisenlohr, F. Ensslen, and D. H. Neuhaus, "Review of technological design options for building integrated photovoltaics (BIPV)," *Energy Build.* **231**, 110381 (2021).
2. H. Lee and H.-J. Song, "Current status and perspective of colored photovoltaic modules," *WIREs Energy Environ.* **10**(6), e403 (2021).
3. G. Eder, G. Peharz, R. Trattnig, P. Bonomo, E. Saretta, F. Frontini, C. S. Polo López, H. R. Wilson, J. Eisenlohr, and N. M. Chivelet, *COLOURED BIPV Market, Research and Development*, 2019.
4. C. Kutter, B. Bläsi, H. R. Wilson, T. Kroyer, M. Mittag, O. Höhn, and M. Heinrich, "Decorated Building-Integrated Photovoltaic Modules: Power Loss, Color Appearance and Cost Analysis," in *Proceedings of the 35rd European Photovoltaic Solar Energy Conference and Exhibition (EUPVSEC)* (2018), pp. 1488–1492.
5. J. Escarré, H.-Y. Li, L. Sansonnens, F. Galliano, G. Cattaneo, P. Heinsteins, S. Nicolay, J. Bailat, S. Eberhard, C. Ballif, and L.-E. Perret-Aebi, "When PV modules are becoming real building elements: White solar module, a revolution for BIPV," in *Proceedings of the 42nd IEEE Photovoltaic Specialists Conference (PVSC)* (IEEE Service Center, 2015), pp. 1–2.
6. V. Caer and A. Schüler, Laminated glazing with coloured reflection and high solar transmittance suitable for solar energy systems, US20150249424 A1.
7. A. Schüler, M. Joly, and V. H. Le Caër, Interference filter with angular independent orange colour of reflection and high solar transmittance, suitable for roof-integration of solar energy systems, WO2014045144A1.
8. J. C. Ortiz Lizcano, P. Procel, A. Calcabrini, G. Yang, A. Ingenito, R. Santbergen, M. Zeman, and O. Isabella, "Colored optic filters on c-Si IBC solar cells for building integrated photovoltaic applications," *Prog. Photovoltaics* **30**(4), 401–435 (2022).
9. O. Höhn, B. Bläsi, T. Kroyer, A. Hinsch, and T. Kuhn, Glazing unit, process for their preparation and their use, DE102017203105B4.
10. B. Bläsi, T. Kroyer, T. Kuhn, and O. Höhn, "The MorphoColor Concept for Colored Photovoltaic Modules," *IEEE J. Photovoltaics* **11**(5), 1305–1311 (2021).
11. T. Starkey and P. Vukusic, "Light manipulation principles in biological photonic systems," *Nanophotonics* **2**(4), 289–307 (2013).
12. P. Vukusic and J. R. Sambles, "Shedding light on butterfly wings," in *Proc. of SPIE*, Proceedings of SPIE (SPIE, 2001), p. 85.
13. G. I. Pokrowski, "Zur Theorie der diffusen Lichtreflexion," *Eur. Phys. J. A* **30**(1), 66–72 (1924).
14. W. E. K. Middleton and A. G. Mungall, "The Luminous Directional Reflectance of Snow*," *J. Opt. Soc. Am.* **42**(8), 572 (1952).
15. K. E. Torrance and E. M. Sparrow, "Theory for Off-Specular Reflection From Roughened Surfaces*," *J. Opt. Soc. Am.* **57**(9), 1105 (1967).
16. B. G. Smith, "Geometrical shadowing of a random rough surface," *IEEE Trans. Antennas Propag.* **15**(5), 668–671 (1967).
17. R. L. Cook and K. E. Torrance, "A Reflectance Model for Computer Graphics," *ACM Trans. Graph.* **1**(1), 7–24 (1982).
18. B. Walter, S. R. Marschner, H. Li, and K. E. Torrance, "Microfacet Models for Refraction through Rough Surfaces," in *Rendering techniques 2007* (Eurographics Association, 2007), pp. 195–206.
19. E. Heitz, "Understanding the Masking-Shadowing Function in Microfacet-Based BRDFs," *Journal of Computer Graphics Techniques* **3**, 32–91 (2014).
20. H. A. Macleod, *Thin-film optical filters*, 4th (CRC Press Taylor & Francis, 2010).
21. D. Depla and S. Mahieu, *Reactive sputter deposition* (Springer, 2008).
22. N. Tucher, J. Eisenlohr, H. Gebrewold, P. Kiefel, O. Höhn, H. Hauser, J. C. Goldschmidt, and B. Bläsi, "Optical simulation of photovoltaic modules with multiple textured interfaces using the matrix-based formalism OPTOS," *Opt. Express* **24**(14), A1083 (2016).
23. N. Tucher, J. Eisenlohr, P. Kiefel, O. Höhn, H. Hauser, I. M. Peters, C. Müller, J. C. Goldschmidt, and B. Bläsi, "3D optical simulation formalism OPTOS for textured silicon solar cells," *Opt. Express* **23**(24), A1720 (2015).
24. N. Tucher, J. Eisenlohr, P. Kiefel, O. Höhn, H. Hauser, I. M. Peters, C. Müller, J. C. Goldschmidt, and B. Bläsi, "Optical properties of textured sheets: an efficient matrix-based modelling approach," in *Proc. of SPIE*, Vol. 9630 of Proceedings of SPIE (SPIE, 2015), p. 96300.
25. Deutsches Institut für Normung e. V., *Farbmetrik — Teil 4: CIE 1976 L*a*b* Farbenraum (ISO/CIE 11664-4:2019)* (11664-4:2019) (Beuth Verlag GmbH, 2020).
26. IEC, Multimedia systems and equipment - Colour measurement and management. Part 2-1: Colour management - Default RGB colour space - sRGB (IEC 61966-2-1:1999) (1999).